${journal.abbrev} 2008.1:883-909. Downloaded from arjournals.annualreviews.org
by HARVARD UNIVERSITY on 10/14/08. For personal use only.

ANNUAL REVIEWS **Further**

**Click here** for quick links to Annual Reviews content online, including:

- Other articles in this volume
- Top cited articles
- Top downloaded articles
- Our comprehensive search

# Coherent Anti-Stokes Raman Scattering Microscopy: Chemical Imaging for Biology and Medicine

Conor L. Evans and X. Sunney Xie

Department of Chemistry and Chemical Biology, Harvard University, Cambridge, Massachusetts 02138; email: xie@chemistry.harvard.edu

Annu. Rev. Anal. Chem. 2008. 1:883–909

The *Annual Review of Analytical Chemistry* is online at anchem.annualreviews.org

This article's doi:
10.1146/annurev.anchem.1.031207.112754

Copyright © 2008 by Annual Reviews.
All rights reserved

1936-1327/08/0719-0883$20.00

## Key Words

Raman, CARS, molecular imaging, biomedical imaging, metabolic imaging, skin imaging

## Abstract

Coherent anti-Stokes Raman scattering (CARS) microscopy is a label-free imaging technique that is capable of real-time, nonperturbative examination of living cells and organisms based on molecular vibrational spectroscopy. Recent advances in detection schemes, understanding of contrast mechanisms, and developments of laser sources have enabled superb sensitivity and high time resolution. Emerging applications, such as metabolite and drug imaging and tumor identification, raise many exciting new possibilities for biology and medicine.

${journal.abbrev} 2008.1:883-909. Downloaded from arjournals.annualreviews.org
by HARVARD UNIVERSITY on 10/14/08. For personal use only.

## 1. INTRODUCTION

Advances in optical imaging techniques have revolutionized our ability to study the microscopic world. Simple microscopy techniques, such as bright field and differential interference contrast microscopy, have played a large role in cellular and molecular biology experiments but do not provide chemical specificity. Imaging modalities capable of identifying specific molecules have significantly improved our understanding of biological processes on the microscopic scale. Many of these techniques, however, require the use of exogenous labels that often perturb the system of interest. Intrinsic imaging techniques such as native fluorescence imaging (1) offer molecular specificity, but the number of endogenous fluorophores are limited.

Vibrational microscopy techniques offer intrinsic chemical selectivity, as different molecules have specific vibrational frequencies. Infrared microscopy (2) has seen rapid development, but it is limited by a number of difficulties including low sensitivity due to non-background-free detection, low spatial resolution associated with the long infrared wavelengths, and water absorption of the infrared light. Raman microscopy has been extensively explored and has found biomedical applications in glucose detection (3), tumor diagnostics (4, 5), DNA detection (6), and microendoscopy (7), among others (**Figure 1**).

Raman microscopy does, however, have a major limitation. The Raman effect is extremely weak (typical photon conversion efficiencies for Raman are lower than 1 in

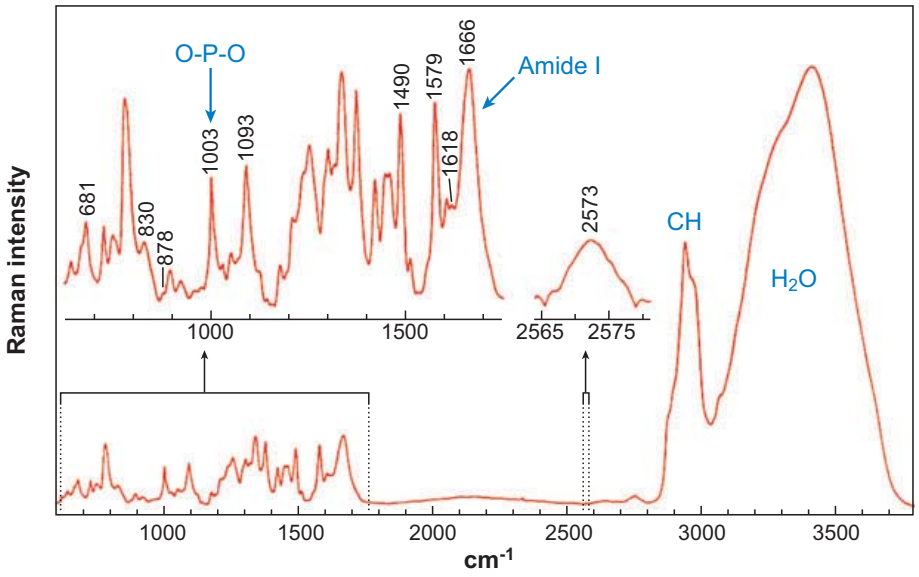


**Figure 1**

The Raman spectrum of the P22 virus showing characteristic vibrational frequencies observed in biological samples. Several vibrational modes of particular interest in vibrational microscopy are labeled (*blue*). The O-P-O stretching vibration arises from the vibration of the DNA backbone. The amide-I band is characteristic of proteins and can be used to map out protein density. The CH-stretching band is typically used to image lipids in biological samples. The $H_2O$-stretching vibrations of water are important for following water flow and density. Adapted with permission from Reference 79.

${journal.abbrev} 2008.1:883-909. Downloaded from arjournals.annualreviews.org
by HARVARD UNIVERSITY on 10/14/08. For personal use only.

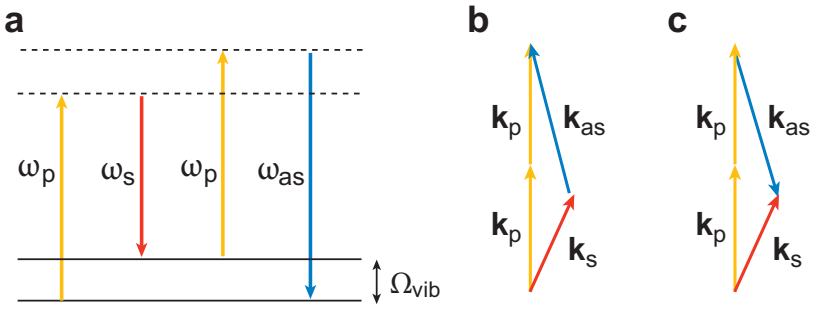


**Figure 2**

(*a*) Diagram of the coherent anti-Stokes Raman scattering (CARS) process. When the difference between the pump and Stokes frequencies ($\omega_p - \omega_s$) matches the molecular vibrational frequency, $\Omega_{vib}$, the anti-Stokes signal is generated at a frequency $\omega_{as} = 2\omega_p - \omega_s$. (*b*) Phase-matching condition for forward-generated CARS. (*c*) Phase-matching condition for backward- (epi-)generated CARS. $k$ is known as the wavevector, and is given by $k = 2\pi / \lambda$. Here, $k_p$, $k_s$, and $k_{as}$ represent the pump, Stokes, and anti-Stokes wavevectors, respectively.

$10^{18}$); therefore, data acquisition times are long. Raman microscopy images require high laser powers and long integration times of 100 ms to 1 s per pixel (8). These factors severely limit the application of Raman microscopy to the study of living systems.

Far stronger vibrational signals can be obtained with coherent anti-Stokes Raman scattering (CARS), which was first reported by Maker and Terhune at the Ford Motor Company in 1965 (9). Ironically, it was not named CARS until almost ten years later (10). In the CARS process, a pump beam at frequency $\omega_p$ and a Stokes beam at frequency $\omega_s$ interact with a sample via a wave-mixing process. When the beat frequency $\omega_p - \omega_s$ matches the frequency of a Raman active molecular vibration, the resonant oscillators are coherently driven by the excitation fields, thereby generating a strong anti-Stokes signal at $\omega_{as} = 2\omega_p - \omega_s$ (**Figure 2**).

The Reintjes group at the Naval Research Laboratory was the first to use CARS as a contrast mechanism for microscopy (11). Due to technical difficulties there were no further developments until 1999, when CARS microscopy was revived at Pacific Northwest National Laboratory (12) with a new method. Since then, CARS microscopy has been used to visualize living cells with contrast of different vibrational modes, including the phosphate stretch vibration (DNA), amide I vibration (protein) (13), OH stretching vibration (water) (14), and the CH group of stretching vibrations (lipids) (15, 16). Among these modes, the signal from lipids is so high that single phospholipid bilayers can be visualized (17, 18). Meanwhile, CARS has proved to be a powerful imaging modality for studying tissues in vivo (19, 20).

The advantages of CARS are summarized as follows:

1. It provides contrast based on the intrinsic molecular vibrations of a specimen, circumventing the need for extrinsic labels.
2. It is orders of magnitude more sensitive than spontaneous Raman microscopy (21–23), permitting video-rate vibrational imaging at moderate excitation powers.

**CARS:** coherent anti-Stokes Raman scattering

${journal.abbrev} 2008.1:883-909. Downloaded from arjournals.annualreviews.org
by HARVARD UNIVERSITY on 10/14/08. For personal use only.

3. The nonlinear nature of the CARS process automatically grants it the capability of three-dimensional sectioning (12), which is essential for imaging thick tissues or cellular structures.
4. The anti-Stokes signal is blue-shifted from the pump and Stokes frequencies, and is therefore easily detected in the presence of one-photon fluorescence.
5. When using near-infrared excitation wavelengths, CARS microscopy can penetrate to depths of nearly 0.4 mm, allowing imaging in thick tissues.
6. As the CARS process occurs on the ground electronic state, sample photodamage is minimized (19), especially when picosecond pulses are used to reduce multiphoton effects.

In this article we summarize some of the recent advances in CARS microscopy, with an emphasis on new applications in the biomedical sciences. In Section 2 we review the fundamentals of CARS microscopy, and in Section 3 we discuss laser sources. Sections 4 and 5 focus on recent innovations and applications of CARS to cellular and biological imaging.

## 2. CARS SPECTROSCOPY

In CARS, the pump and Stokes fields coherently drive all resonant oscillators in the excitation volume at $\omega_p - \omega_s$ with a well-defined phase. The coherent superposition of the microscopic induced dipoles generates a macroscopic third-order polarization $P^{(3)}$ at the anti-Stokes frequency. The anti-Stokes field arises from the nonlinear interactions of the pump and Stokes fields, $E_p$ and $E_s$, respectively, and is given by $P^{(3)}(\omega_{as}) \propto \chi^{(3)} E_p^2 E_s^*$, where the complex proportionality constant $\chi^{(3)}$ is known as the third-order susceptibility. By solving the wave equation, assuming plane pump and Stokes waves, one obtains the anti-Stokes signal intensity,

$$I_{AS} \propto \left|\chi^{(3)}\right|^2 I_p^2 I_s \left(\frac{\sin(\Delta k z/2)}{\Delta k/2}\right)^2 \quad (1)$$

where $z$ is the sample thickness, $k_i = 2\pi/\lambda_i$ is the wavevector, and $\Delta k$, the wavevector mismatch, is defined as $\Delta k = k_{as} - (2k_p - k_s)$ and gives the velocity difference of the three frequencies. The sinc function is maximized when $\Delta k z$ is close to zero, which is known as the phase-matching condition. **Figure 2*b*,*c*** shows the phase-matching conditions for forward- and backward (epi)-detected CARS signal. Although $\chi^{(3)}$ is linearly dependent on the number of oscillators, the CARS signal depends upon $|\chi^{(3)}|^2$ and is therefore proportional to the square of the number of vibrational oscillators. This makes CARS different from Raman, which is linearly dependent on the number of vibrational oscillators (24).

Even when $\omega_p - \omega_s$ is tuned far from vibrational resonances, the pump and Stokes fields can induce a macroscopic polarization at the anti-Stokes frequency due to the electronic response of the material. When $\omega_p$ and $\omega_s$ are far from electronic resonance, this polarization leads to a vibrationally nonresonant contribution to the CARS signal. When $\omega_p - \omega_s$ is tuned to a particular vibrational frequency, the anti-Stokes signal is enhanced. Therefore, $\chi^{(3)}$ has two terms, one resonant ($\chi_R^{(3)}$) and one

nonresonant ($\chi^{(3)}_{NR}$):

$$\chi^{(3)} = \chi^{(3)}_{NR} + \frac{\chi^{(3)}_R}{\Delta - i\Gamma}, \tag{2}$$

where $\Delta$ is the detuning $\Delta = \omega_p - \omega_s - \Omega_R$ (Raman shift), and where $\Omega_R$ is the center frequency of a homogenously broadened Raman line with bandwidth $\Gamma$.

${journal.abbrev} 2008.1:883-909. Downloaded from arjournals.annualreviews.org
by HARVARD UNIVERSITY on 10/14/08. For personal use only.

## 2.1. Contributions to the CARS Response

As the CARS intensity is proportional to $\left|\chi^{(3)}\right|^2$, the intensity of the anti-Stokes signal can be written as:

$$I_{CARS}(\Delta) \propto \left|\chi^{(3)}_{NR}\right|^2 + \left|\chi^{(3)}_R(\Delta)\right|^2 + 2\chi^{(3)}_{NR}\,\mathrm{Re}\,\chi^{(3)}_R(\Delta), \tag{3}$$

where Re $\chi^{(3)}_R$ is the real part of resonant term of $\chi^{(3)}$. The first term is independent of the Raman shift, and is known as the nonresonant background. The second term contains only resonant information, and is the dominant contribution when probing strong and/or concentrated resonant scatterers. Mixing between the nonresonant and resonant contributions creates the third term, which contains the real part of the vibrational response. Plotted in **Figure 3*a*** is the spectral response of each term, showing its individual contribution. As the shape of the third term is dispersive, the addition of the three terms creates a redshift of the maximum of the CARS spectral peak and causes a negative dip at the blue end (25) (**Figure 3*b***). The redshift in peak position, which depends upon the relative intensity of the resonant and nonresonant contributions, makes it difficult to apply the wealth of information in Raman literature to assigning CARS spectra (26).

The nonresonant contribution also introduces an offset that gives CARS microscopy images a background (**Figure 3*c*,*d***). The blue-end dip is not desirable as it gives negative contrast (**Figure 3*e***). Spectral interference between two or more resonances can result in distorted line shapes, and precludes an immediate quantitative interpretation of the spectrum, as the neighboring peaks influence one another's intensity. In congested spectral regions, this leads to nearly uninterpretable CARS spectra. It is possible to glean Raman spectra from the CARS signal by extracting the $\chi^{(3)}$ through interferometry (21, 22), although such methods can complicate a CARS imaging system.

## 2.2. Imaging versus Spectroscopy

Although it would be ideal to collect a complete spectrum for every object in a CARS microscopy image, in practice these are difficult to obtain. In recent CARS microspectroscopy experiments, a broadband femtosecond laser source is used in conjunction with a monochromator to collect pixel-by-pixel spectroscopic data (27, 28). This results in integrations times of milliseconds to seconds per pixel for many samples, causing significant photodamage. In addition, current detectors used in spectroscopy experiments have long readout times that limit their acquisition speed. These limits currently cap CARS microspectroscopy imaging experiments to frame rates of several minutes for 256 × 256 pixel image (29, 30). Such acquisition rates are too slow for

${journal.abbrev} 2008.1:883-909. Downloaded from arjournals.annualreviews.org
by HARVARD UNIVERSITY on 10/14/08. For personal use only.

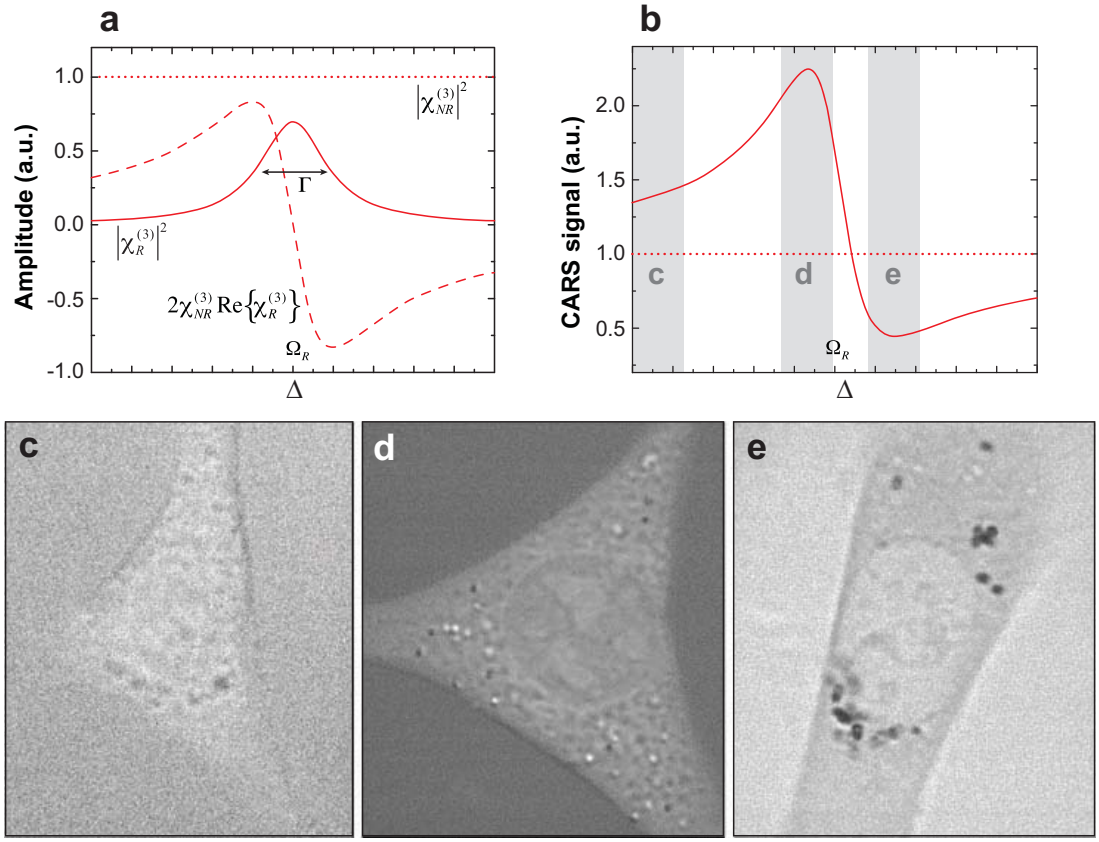


**Figure 3**

(*a*) Three components of the coherent anti-Stokes Raman scattering (CARS) signal plotted as a function of detuning. Shown here are the purely resonant term (*solid line*), the nonresonant background term (*dotted line*), and the mixing term (with a dispersive shape) (*dashed line*). The plotted curves were calculated for $\chi_{NR}^{(3)} = 1.2\,\chi_R^{(3)}(\Delta = 0)$. (*b*) The total CARS signal. The solid line represents the sum of the contributions from panel *a*, while the dotted line represents the nonresonant background. (*c–d*) Forward-propagating CARS images of 3T3-L1 cells that display contrast corresponding to the highlighted regions of Raman shifts in panel *b*. Panel *c* presents a cell imaged off resonance; only nonresonant contrast is observed. Panel *d* shows a cell imaged at 2845 $cm^{-1}$, the $CH_2$ symmetric stretching vibration. Numerous lipid bodies, including lipid droplets, can be seen. (*e*) Cell imaged at the blue dip of the CH-stretching band at 2950 $cm^{-1}$. Resonant features appear dark against the nonresonant background.

most biomedical experiments and are prohibitive for studying dynamics in biological systems. Even when a spectrum can be collected, it cannot immediately be translated to quantitative information without significant off-line processing (31).

We believe that it is best to utilize a narrowband imaging approach for high-resolution CARS microscopy. Instead of collecting a spectrum at each point in the image, one can collect an image for selected points in the spectrum. Doing so capitalizes on the strength of the CARS response, allowing for vibrationally selective imaging with high time resolution. By tuning in the laser system to only one resonance, CARS microscopy can be carried out at video-rate speeds (19) with diffraction-limited resolution. This narrowband approach has far greater applicability as a biomedical

imaging technique than broadband excitation schemes (29–34). Many specimens, such as tissues, are highly scattering and easily distort the spectral phase and polarization properties needed for broadband interferometric techniques. Narrowband CARS microscopy has been widely applied, is not limited to thin or weakly scattering samples, and has the capability for future use in clinical settings as an in situ imaging technique.

**NA:** numerical aperture

${journal.abbrev} 2008.1:883-909. Downloaded from arjournals.annualreviews.org
by HARVARD UNIVERSITY on 10/14/08. For personal use only.

## 2.3. Tight Focusing Relaxes the Phase-Matching Condition

The first CARS microscope was built using a nonlinear geometry (11). This cross-beam arrangement, however, suffered from low spatial resolution and sensitivity, and its complexity was not ideal for a microscopic imaging modality. It was not until 1999 that a discovery cleared the way for modern CARS microscopy (12). The effective axial point spread function for near-infrared (NIR) light used with a high numerical aperture (NA) lens (>0.8) is about 1 μm long. As the NA becomes larger than 0.2, the $\text{sinc}^2$ function in Equation 1 asymptotically approaches a maximum, rendering non-collinear phase-matching geometries, such as BOXCARS unnecessary. Therefore, it is possible to use a collinear pump and Stokes beams to generate anti-Stokes signal at the tight focus. These collinear beams are raster-scanned over a sample using commercial confocal scanning microscopes (13) (**Figure 4*a***).

## 2.4. Forward- and Epi-CARS Generation Mechanisms

Due to the coherent nature of the signal buildup in CARS, the far-field radiation pattern is more complicated than those observed in incoherent imaging techniques such as fluorescence and Raman microscopy, where the signal is emitted in all directions. The radiation pattern in CARS microcopy is highly dependent on a number of parameters, including the size and shape of the scattering objects, the nonlinear susceptibilities of the object, and the local environment (35). Each vibrationally oscillator can be considered as a Hertzian dipole at the anti-Stokes frequency (**Figure 5*a***). For extremely thin slabs of oscillators, the radiation pattern becomes more directional, and propagates equally in the forward and epi directions (**Figure 5*b***). As the sample thickness, $z$, increases, constructive interference occurs in the forward direction (36) (**Figure 5*c***), as $\Delta k$ is small (**Figure 2*b***), resulting in forward-propagating CARS (F-CARS). At the same time, destructive interference occurs in the backward direction as $\Delta k$ is large (**Figure 2*c***) (35, 37), leading to no epi-CARS signal for bulk objects (**Figure 5*d***).

It would seem, then, that the CARS signal would be generated in the forward direction only. This is not the case, however, as epi-directed signal (38) has been observed in CARS microscopy arising from three different mechanisms. In the first mechanism, epi-CARS signal is generated from objects whose size is small enough ($\lambda_p/3$) for incomplete destructive interference to occur in the backward direction. If the size of scatterer is larger, the epi-directed fields from dipoles across the object run out of phase with each other, leading to destructive interference of the epi-CARS signal (**Figure 5*e***). We note that the phase-matching condition still holds for this mechanism; while $\Delta k$ is large, the path length, $z$, is small enough to maximize the sinc function of Equation 1. In the second mechanism for epi-CARS generation,

${journal.abbrev} 2008.1:883-909. Downloaded from arjournals.annualreviews.org
by HARVARD UNIVERSITY on 10/14/08. For personal use only.

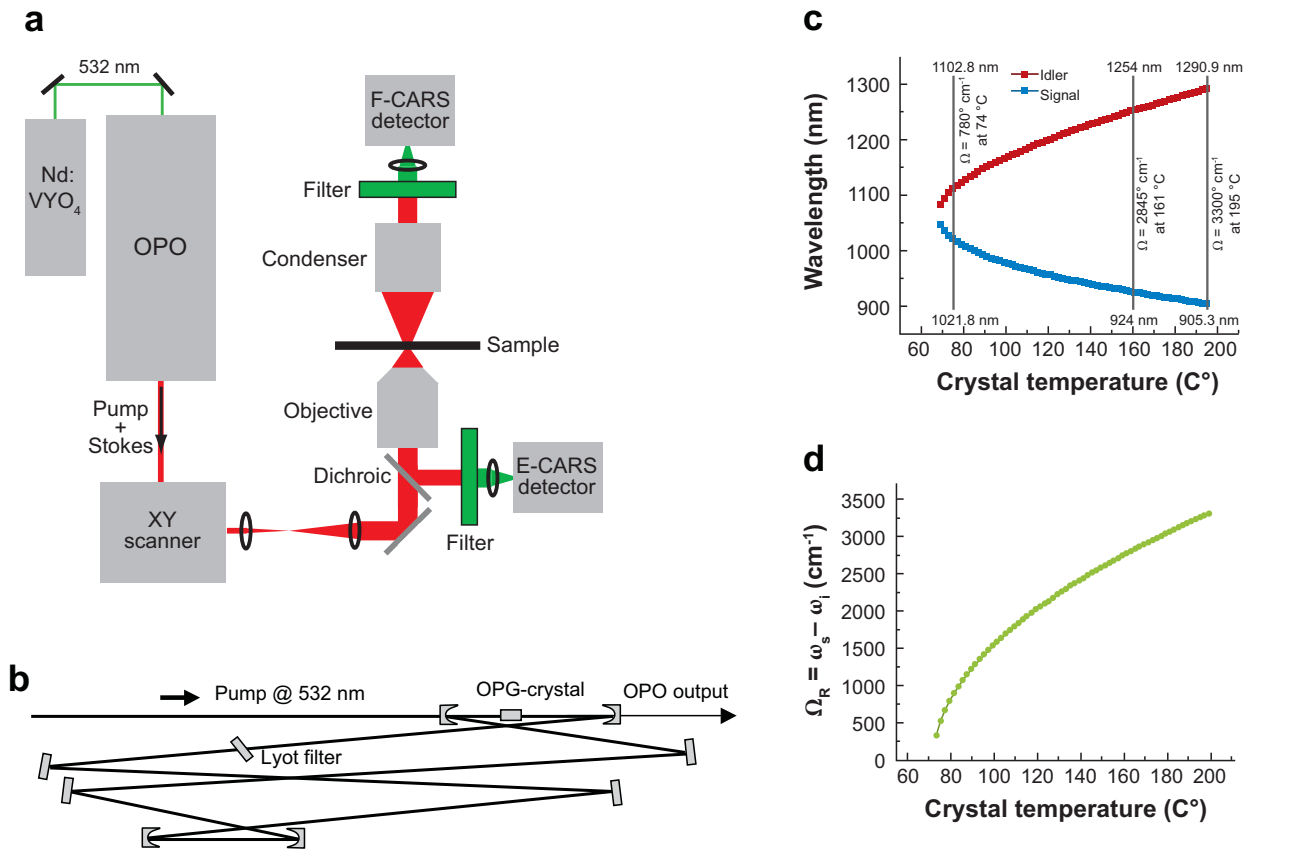


**Figure 4**

(*a*) Diagram of a collinear beam-scanning coherent anti-Stokes Raman scattering (CARS) microscope. An Nd:Vanadate laser pumps a dual-wavelength optical parametric oscillator (OPO). The combined pump and Stokes beam from the OPO is raster-scanned over the sample by an *XY* scanner, typically a set of galvanometric mirrors. The CARS signal generated in the forward direction is collimated by a condenser, separated from the excitation beams by a filter, and focused onto a detector for collection. The epi-CARS signal is detected by a large area detector placed after a filter, or by a descanned detector in a manner similar to epi-fluorescence detection (not shown). (*b*) Cavity design for the dual-wavelength OPO. Both noncritically phase-matched LBO ($LiB_3O_5$) and PP-KTP (periodically poled $KTiOPO_4$) crystals have been successfully used for parametric downconversion. When LBO is used, the output wavelengths can be simultaneously tuned from 670 nm to 980 nm for the signal and 1100 nm to 1350 nm for the idler. Fine-wavelength tuning is accomplished using a Lyot filter set at Brewster's angle. (*c*) Signal and idler tuning curves as a function of temperature for a PP-KTP based OPO. (*d*) Energy difference between the signal and idler frequencies as a function of crystal temperature for PP-KTP. Abbreviation: F-CARS, forward-propagating coherent anti-Stokes Raman scattering.

backward-propagating anti-Stokes signal is generated at sharp discontinuities in $\chi^{(3)}$. Edges or discontinuities give rise to epi-CARS signal, as they are essentially infinitely small objects that break the symmetry of the focal volume (35) (**Figure 5*b*,*f***). There is a third mechanism for generating epi-directed photons, although it is not related to coherent signal buildup. In this mechanism, a sample that contains many local changes in the index of refraction can redirect forward-propagating photons in the

${journal.abbrev} 2008.1:883-909. Downloaded from arjournals.annualreviews.org
by HARVARD UNIVERSITY on 10/14/08. For personal use only.

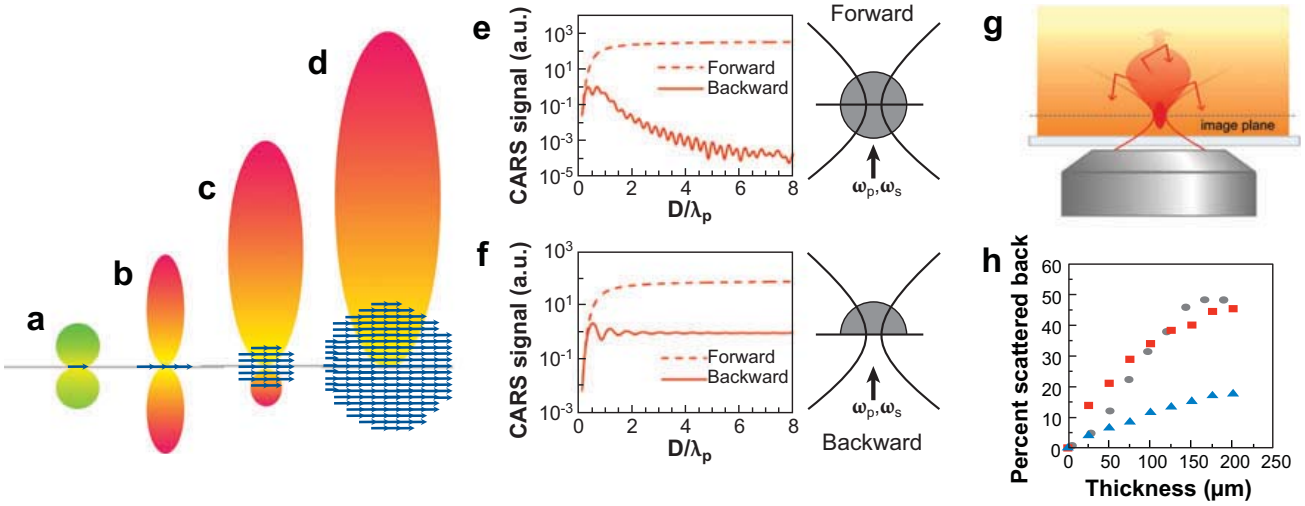


**Figure 5**

The effects of coherent signal buildup in the focal volume. (*a*) The radiation pattern of a single oscillating dipole sends equal intensities in both the forward and backward (epi) directions. (*b*) The fields from a plane of dipoles coherently add to generate equal signal levels in the forward and epi directions. (*c*) A few induced dipoles together generate a forward-propagating component as well as a weak epi-directed signal. (*d*) Many dipoles in the focal spot, such as in bulk material, coherently interfere to generate only a strong forward signal. (*e*) As the size of the scattering object increases, the epi signal generated by Mechanism I drops dramatically while the forward signal continues to build to an asymptotic level defined by the focal volume. Adapted from Reference 35 with permission. (*f*) At an interface, Mechanism II generates an epi signal that is constant in intensity once the object size exceeds the focal volume. (*g*) Mechanism III: Forward-propagating coherent anti-Stokes Raman scattering (F-CARS) photons can be backscattered by a turbid sample and redirected in the epi direction. (*h*) Collection efficiency of epi detection by Mechanism III as a function of sample thickness in a tissue phantom (intralipid suspension) and mouse skin tissue (19). The focus was placed 1 μm deep for both theory and experiment. Shown are the percentage of forward signals redirected backward as the thickness of the intralipid layer was increased (*gray dots*); the results of a Monte Carlo simulation of the experiment (*red squares*); and a curve calculated by the same Monte Carlo simulation, this time using the tissue parameters of mouse skin ($\mu_s = 150\ \text{cm}^{-1}$, $\mu_a = 0.1\ \text{cm}^{-1}$, and $g = 0.85$) (*blue triangles*). Nearly 15% of the F-CARS signal generated in mouse skin was estimated to scatter backward.

epi direction. In turbid samples such as skin, initially forward-propagating photons undergo multiple linear scattering events, which redirect a large number of photons back toward the objective (**Figure 5*g***). This mechanism was found to be the primary contributor to epi-CARS signal from tissues (19) (**Figure 5*h***). We note that the backward signal collected by the objective, which is often out of focus, is only generated at the laser excitation volume.

## 3. LASER SOURCES FOR CARS

Recent advances in CARS microscopy have been facilitated by the development of new light sources. We believe that the ideal sources for CARS microscopy are picosecond tunable pulsed laser systems operating in the NIR.

${journal.abbrev} 2008.1:883-909. Downloaded from arjournals.annualreviews.org
by HARVARD UNIVERSITY on 10/14/08. For personal use only.

### 3.1. Laser Parameters

An important consideration for laser wavelength choice is the nonresonant background. Nonresonant CARS signal can be generated when the pump wavelength is near the peak of a two-photon resonance. Sources in the NIR minimize these two-photon interactions and therefore provide images with better signal-to-noise ratios. Another advantage of using NIR laser sources is low multiphoton absorption–induced photodamage. Multiphoton (typically two-photon) absorption is the major cause of sample damage in most samples (16, 39). CARS sources employing pump beams shorter than 800 nm can generate a large amount of multiphoton absorption by ultraviolet electronic resonances. Researchers have found that most multiphoton damage significantly decreases when the pump wavelength is raised above 800 nm (19, 39).

Near-infrared excitation has another advantage. Tissue samples are typically highly scattering, limiting the penetration depth of CARS microscopy. As the pump and Stokes beams converge in a specimen, scattering in the tissue leads to a loss of laser intensity accompanied by an increase in the focal spot size (40). This results in a deteriorated CARS signal due to its nonlinear intensity dependence. The reduced scattering experienced by NIR pump and Stokes wavelengths maximizes the sample penetration depth, allowing for deep CARS imaging even in turbid samples.

Pulsed lasers systems are needed as CARS signal scales cubically with the intensity of the incident laser light. As such, the choice of pulse width is worthy of careful consideration. Vibrational linewidths are typically on the order of 10–20 $cm^{-1}$, whereas ~100-fs-duration pulses are about 150 $cm^{-1}$ in bandwidth in the near IR. A femtosecond pulsed system centered on a resonance will, therefore, use only a small part of its spectral components to pump the narrow Raman line, but will generate a large nonresonant background signal that often obscures chemically specific contrast. Moreover, because the nonresonant signal coherently mixes with the resonant signal of interest, it cannot simply be subtracted from an image. A good compromise between signal strength and spectral resolution is to use pulses ~3 ps in duration (38). **Table 1** lists our recommendations for optimum laser parameters for CARS microscopy.

**Table 1 Parameters of laser light sources for CARS microscopy**

| Parameter | Optimal Range |
|---|---|
| Pump wavelength range | 780–980 nm |
| Stokes wavelength range | 1000–1300 nm |
| Pulse duration | 2–7 ps |
| Spectral bandwidth | 3–5 $cm^{-1}$ |
| Pulse energy | 0.1–1 nJ |
| Pulse repetition rate | 50–100 MHz |

${journal.abbrev} 2008.1:883-909. Downloaded from arjournals.annualreviews.org
by HARVARD UNIVERSITY on 10/14/08. For personal use only.

### 3.2. Optimum Laser Sources for CARS Microscopy

Our latest CARS source was introduced by Ganikhanov et al. (41) and uses the signal and idler outputs of an optical parametric oscillator (OPO) as the pump and Stokes frequencies, respectively, for CARS microscopy. The most recent design (**Figure 4*b***) is a broadly tunable picosecond OPO (commercialized as the Levante Emerald by APE-Berlin), based on a noncritically phase-matched crystal for parametric down-conversion, and is synchronously pumped by the second-harmonic (532 nm) output of a mode-locked Nd:$YVO_4$ laser (HighQ Laser, Austria). The signal and idler frequencies are continuously temperature tunable about the degeneracy point (signal and idler wavelengths at 1064 nm) to 670 nm for its signal beam and to 2300 nm for its idler beam, making it possible to cover the entire chemically important vibrational frequency range of 200–3600 $cm^{-1}$ without cavity adjustment (**Figure 4*c*,*d***). Unlike previous light sources such as synchronized Ti:Sapphire lasers (13, 42, 43), the pump (signal) and Stokes (idler) pulse trains are inherently optically synchronized and collinearly overlapped at the output of the OPO. This considerably reduces the complexity of a CARS setup, as the combined output beam can be immediately coupled into a microscope (**Figure 4*a***).

**OPO:** optical parametric oscillator

A drawback of the NIR source is the low spatial resolution of ~350 nm. Additionally, anti-Stokes signal can be generated at wavelengths well into the NIR for many vibrational modes that are not accessible with standard detectors. Fortunately, the wide tuning range of this source enables it to run at two different wavelength regimes. In order to achieve higher-resolution imaging or to reach vibrational bands in the fingerprint region, the signal output of the OPO can be combined with the 1064-nm output of the Vanadate laser. This optically synchronized wavelength pair can achieve a microscopic resolution of 300 nm, and the Raman shift can be tuned as low as 800 $cm^{-1}$. As the OPO essentially delivers the wavelength tunability of two sources, its extreme flexibility allows the study of samples with a range of resolutions and depth penetrations.

Looking into the future, fiber lasers offer great potential as they are simple, reliable, and low in cost compared with free-space systems. Fiber lasers could find use as pump lasers for OPOs, or as sources of pump and Stokes beams directly.

## 4. INCREASING SENSITIVITY

The first three-dimensional CARS microscope in 1999 (12) required nearly 30 minutes to acquire a single image. As of 2008, CARS microscopy systems run at acquisition rates of 30 frames per second, an improvement in sensitivity of over four orders of magnitude. Although many improvements to CARS microscopy have been made over the past few years, it is still limited by the nonresonant background whose fluctuation due to laser noise can often obscure weak resonant signals. Numerous methods have been developed to decrease this nonresonant contribution. Polarization-sensitive detection (44) was developed to completely suppress the nonresonant contribution through polarization control, but the technique significantly

${journal.abbrev} 2008.1:883-909. Downloaded from arjournals.annualreviews.org
by HARVARD UNIVERSITY on 10/14/08. For personal use only.

**FM-CARS:** frequency modulation coherent anti-Stokes Raman scattering

attenuates the resonant signal of interest. Epi-CARS microscopy (45) eliminates the nonresonant background from the bulk material, but not the nonresonant contribution from small scatters. Time-resolved CARS (46) has also been used for nonresonant background rejection, but it is cumbersome to implement. Interferometric CARS approaches, although successful in eliminating the nonresonant background by separating the real and imaginary components of the third-order susceptibility $\chi^{(3)}$ (21, 22, 47), are difficult to use with heterogeneous samples due to index-of-refraction changes. All of the above approaches are limited in sensitivity as polarization, temporal phase, spatial phase, and spectral phase can all be influenced by sample heterogeneity and therefore are not always reliable.

We have developed a more sensitive approach called frequency modulation CARS (FM-CARS). The nonresonant background, $|\chi^{(3)}_{NR}|^2$, the first term in Equation 1, is constant over all Raman shifts and dominates the CARS signal when the resonant signal is weak, i.e. when the second term in Equation 1 is negligible. Under this condition, we exploit the dispersive nature of the mixing term by modulating the Raman shift ($\Delta$) around the center frequency $\Omega_R$. This results in an amplitude modulation of the CARS signal, which can be detected using a lock-in amplifier. By toggling the Raman shift, a resonant spectral feature becomes a frequency modulation (FM) to amplitude modulation (AM) converter (**Figure 6*a***). The spectrally flat nonresonant background does not contribute to the detected modulated signal, and therefore is suppressed. This frequency modulation CARS technique is general enough to be applied to either forward or backward CARS in any sample. Additionally, if the modulation is carried out at rates exceeding 500 kHz, the modulated signal can be separated from laser, mechanical, and most electrical noise sources. Using this approach, FM-CARS

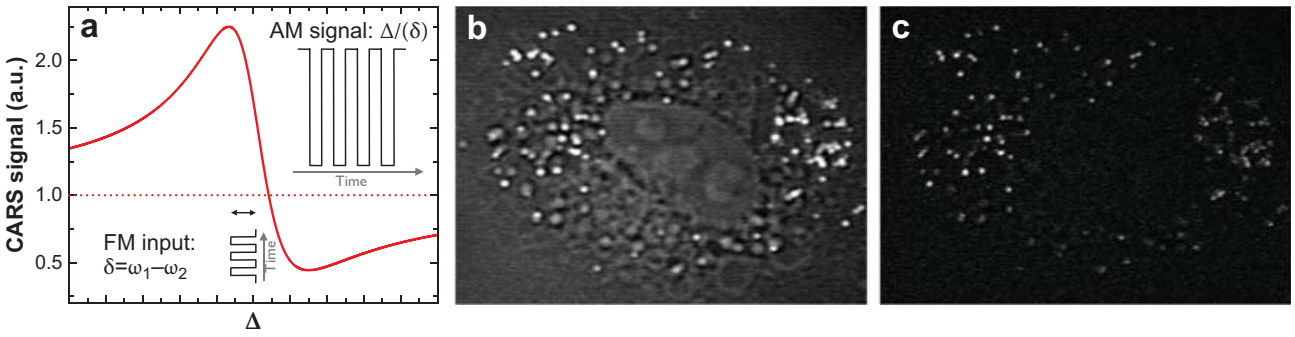


**Figure 6**

(*a*) Schematic of the frequency modulation coherent anti-Stokes Raman scattering (FM-CARS) process. Represented here are the sum of the contributions from **Figure 2*a*** (*solid line*) and the nonresonant background (*dotted line*). The resonance acts as an FM-to-AM converter, resulting in an amplitude-modulated signal that can be detected by a lock-in amplifier. (*b*) Forward-CARS image of a fixed A549 human lung cancer cell cultured with deuterium-labeled oleic acids taken at a Raman shift of 2100 $cm^{-1}$. (*c*) FM-CARS image obtained when toggling between 2060 $cm^{-1}$ and 2100 $cm^{-1}$. Nonresonant background components have been significantly reduced by the FM-CARS method. Abbreviations: FM, frequency modulation; AM, amplitude modulation.

systems have been shown to provide sensitivities nearly three orders of magnitude greater than conventional CARS imaging (23).

As FM-CARS can be easily incorporated into any detection geometry, it can be immediately applied to biomedical imaging. To demonstrate the capabilities of FM-CARS, deuterated lipids were isolated from the nonresonant contribution in human lung cancer cells (23). An F-CARS image of these cells at the $CD_2$ stretching frequency shows a number of cellular features, complicating identification of the cellular components that contain the deuterated oleic acid (OA) (**Figure 6*b***). When FM-CARS is used, however, the nonresonant signal is suppressed and the deuterated components can be easily identified (**Figure 6*c***). Continued progress in FM-CARS promises to improve the sensitivity limit, allowing for future applications such as drug and metabolite imaging that will have significant benefits for cell biology and biomedicine.

**OA:** oleic acid

${journal.abbrev} 2008.1:883-909. Downloaded from arjournals.annualreviews.org
by HARVARD UNIVERSITY on 10/14/08. For personal use only.

## 5. APPLICATIONS OF COHERENT ANTI-STOKES RAMAN SCATTERING MICROSCOPY TO BIOLOGY AND MEDICINE

Developments over the past several years have enabled the application of CARS microscopy to the chemical, materials, biological, and medical fields. Chemical applications include many studies on lipid vesicles (31, 48, 49), lipid layers (50), and the ordering of lipid domains (18, 39). In the materials field, CARS has been used to examine the dynamics of water in organic environments (51, 52) and has been applied to the processing of photoresists (51) and the ordering of liquid crystals (53). The most exciting recent applications of CARS have been in the fields of biological and medical imaging, and are the focus of this section.

### 5.1. Imaging Cells with Chemical Selectivity

CARS provides new views into cellular structures. A recent example is the imaging of plant cells. Plant cell walls are primarily composed of polysaccharides (such as cellulose), lignin, and glycoproteins. Lignin is largely responsible for the resistance to chemical/enzymatic degradation of cellulose into short chain sugar molecules in the process of biomass conversion to biofuel. However, it is difficult to image lignin using conventional imaging methods. In order to improve the conversion efficiency, one requires an imaging technique with contrast based on chemical composition for real-time monitoring. The structure of lignin (**Figure 7*a***) gives rise to a Raman spectrum (**Figure 7*b***) with a band at 1600 $cm^{-1}$ due to the aryl symmetric ring stretching vibration, which can serve as a sensitive probe for lignin. **Figure 7*c*** shows a CARS image of corn stover tuned into the 1600 $cm^{-1}$ stretch, which reveals the distribution of lignin within the walls of individual cells.

Far more work has been done on mammalian cells, where the cellular organelles can be imaged by CARS. The strongest observed signal comes from the CH bonds, which are abundant in lipids. This strong signal allows the observation of dynamic processes with high time resolution. For example, rapid intracellular transport in

${journal.abbrev} 2008.1:883-909. Downloaded from arjournals.annualreviews.org
by HARVARD UNIVERSITY on 10/14/08. For personal use only.

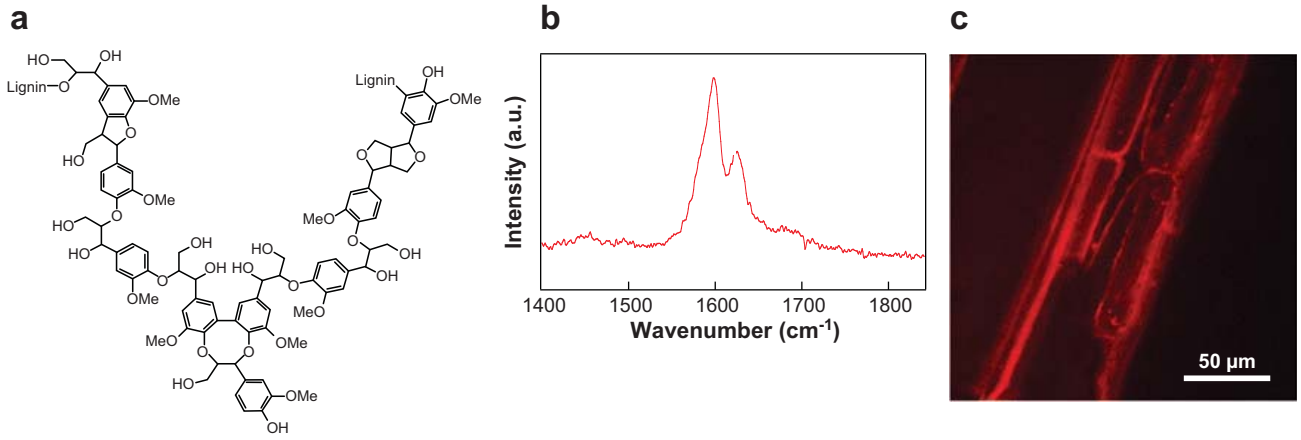


**Figure 7**

(*a*) Chemical structure of the lignin polymer. (*b*) Raman spectrum of lignin, with prominent bands near 1600 $cm^{-1}$ arising from the aryl ring stretching vibrations. (*c*) Coherent anti-Stokes Raman scattering microscope image at 1600 $cm^{-1}$ showing the distribution of lignin in the cell walls surrounding the plant cells in corn stover.

mammalian cells is driven by molecular motors that bind to and move select cellular organelles along the cellular cytoskeleton (54, 55). Organelle trafficking is an essential process, and even small changes to the cellular environment can have large effects on intracellular transport. In particular, the transport of lipid droplets (LDs) (56–58) can be difficult to selectively visualize, as fluorescent LD labels may have perturbative effects (59). CARS microscopy, with its exquisite sensitivity to lipids, has proven to be an excellent tool for LD tracking. In a recent study by Nan et al. (16), CARS microscopy was used to monitor the transport of LDs in steroidogenic Y-1 mouse adrenal cortical cells by tuning into the lipid $CH_2$ stretching frequency (2845 $cm^{-1}$). LDs were observed to undergo caged, subdiffusive motion due to trapping in the cytoskeleton along with the rapid, superdiffusive motion generated by a molecular motor. In particular, a correlation between cell shape and LD transport activity was observed, which is thought to increase the collision rate of LDs with mitochondria for steroidogenesis. It is evident that CARS is complementary to existing microscopy techniques, such as fluorescence microscopy, for interrogating cellular structure and dynamics.

## 5.2. Metabolic Imaging

Metabolites are small molecules that are difficult to image using conventional microscopy techniques. Labels such as fluorophores are typically comparable in size to most metabolites, and will thus significantly alter their behavior in vivo. Knowledge of the transport, delivery, and localization of such molecules is critical for the study of disease and for the development of effective treatments. The vibrational selectivity of CARS microscopy makes it a powerful tool for such studies. For example, CARS microscopy's sensitivity to long-chain hydrocarbons makes it an ideal method for studying the metabolism of lipids. In an early experiment, CARS

${journal.abbrev} 2008.1:883-909. Downloaded from arjournals.annualreviews.org
by HARVARD UNIVERSITY on 10/14/08. For personal use only.

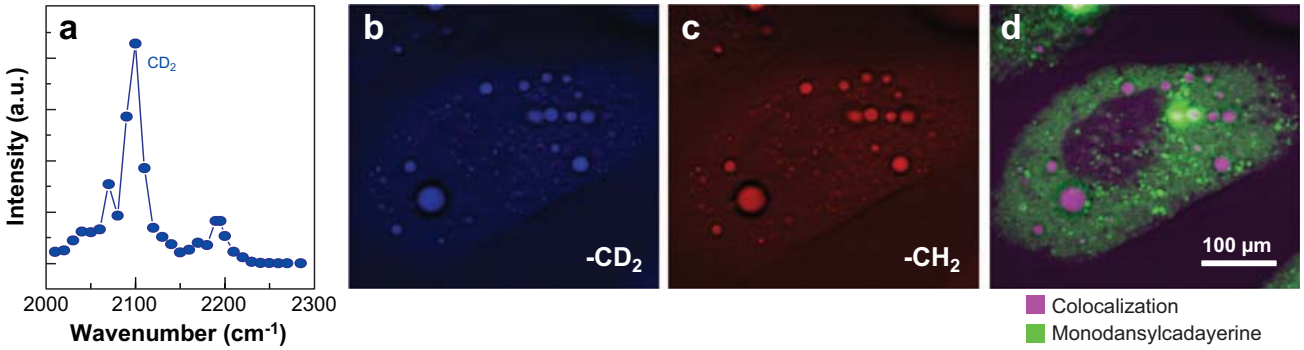


**Figure 8**

Lipid metabolism studied with coherent anti-Stokes Raman scattering (CARS) microscopy. (*a*) The CARS spectrum of deuterated oleic acid. (*b-d*) Rat hepatocyte cells were incubated with both eicosapentaenoic acid and deuterated oleic acid. (*b*) CARS image taken at the $CD_2$ symmetric stretching vibration at 2090 $cm^{-1}$. (*c*) CARS image taken at the $CH_2$ symmetric stretching vibration at 2845 $cm^{-1}$. (*d*) Composite image of panels *b* and *c*, showing colocalization along with two-photon fluorescence from monodansylcadayerine, a label for degradative lysozymes.

was used to follow the differentiation of cells into adipocytes, following the growth of LDs in cells over the course of several days (15). Two recent studies have used CARS microscopy to investigate the changes in lipid metabolism caused by the hepatitis C virus (60, 61). Recent work by Hellerer et al. (62) demonstrates the ability of CARS microscopy to image lipid metabolism in a living organism by monitoring lipid storage in different strains of *Caenorhabditis elegans*.

The above experiments used CH contrast. For many studies, however, a method is needed for imaging a specific small molecule inside cells. Isotope labeling via deuterium substitution has recently been demonstrated as a powerful method (63). The deuterium in a CD bond is heavier than hydrogen, placing CD vibrational stretching frequencies into an otherwise "silent" region of the biological Raman spectra near 2100 $cm^{-1}$ (**Figure 8*a***). By substituting nonreactive hydrogens with deuterium to avoid perturbation and tuning into these unique CD stretching frequencies, it is possible to selectively image a specific molecule using CARS contrast.

This approach was used to selectively image the metabolism of different lipids in a study investigating the effects of omega-3 fatty acids. Fish oil is rich in polyunsaturated fats, such as omega-3 fatty acids, and has been found to affect lipid biochemistry in humans by lowering blood triglyceride levels. To study the effect of omega-3 fatty acids on cellular lipid metabolism, rat hepatoma cells were treated with a combination of normal (OA) and omega-3 (eicosapentaenoic acid, EPA) fatty acids. Because the two molecules have similar CARS spectra, deuterium substitution in OA was used to specifically image the monounsaturated fatty acid. Cells grown with only oleic acid in the culture media were found to sequester OA into small LDs. When cells were cultured only with EPA, the EPA was incorporated into lysosomes (acidic organelles that digest cellular components). Interestingly, when cells were grown with OA and

**EPA:** eicosapentaenoic acid

EPA together, both fatty acids were found colocalized in lysosomes (**Figure 8*b,c,d***), indicating that omega-3 fatty acids such as EPA change the way cells process normal fatty acids (63). This CARS metabolic study, using deuterium substitution for specific nonperturbative labeling, is important for understanding the health benefits of polyunsaturated fatty acids such as omega-3s.

${journal.abbrev} 2008.1:883-909. Downloaded from arjournals.annualreviews.org
by HARVARD UNIVERSITY on 10/14/08. For personal use only.

## 5.3. Biomedical Imaging

Over the past several years, many applications of CARS microscopy to biomedicine have emerged. CARS imaging is especially useful for in vivo and in situ investigations, wherein the use of selective labels might be impossible or prohibitive. Compared to techniques such as magnetic resonance imaging, CARS does not have a large penetration depth; instead, it offers subcellular spatial resolution and high time resolution.

CARS imaging in vivo was first demonstrated on the skin of a mouse, and utilized a real-time video-rate CARS imaging system (19). By tuning into the $CH_2$ vibrational stretching frequency, CARS microscopy was able to visualize the abundant lipid structures throughout the 120-μm depth of mouse ear skin. At the skin surface, the bright polygonal stratum corneum was visible due to the presence of the intracellular "mortar" that holds the many surface corneocytes together. This intracellular material is rich in lipids, ceramides, and cholesterol and gave rise to a strong CARS signal (**Figure 9*a***). Multicellular sebaceous glands appeared 20 μm below the surface of the skin (**Figure 9*b***). These glands are packed with micrometer-sized granules of sebum, a compound rich in triglycerides and wax esters (**Figure 9*e***). At depths of 60 μm, large adipocytes were clearly visible, many aligned along blood vessels (**Figure 9*c***). At the bottom of the dermis, small adipocytes forming the subcutaneous fat layer could be seen (**Figure 9*d***). The use of a video-rate CARS imaging system allowed for rapid, three-dimensional reconstruction of the entire tissue depth (**Figure 9*f***). This study was also able to track, in real time, chemical diffusion into skin by following the application of baby oil.

Recent studies have investigated the transdermal delivery of retinol, a drug that stimulates collagen growth in skin. The conjugated polyene structure of the drug (**Figure 10*a***) gives rise to a strong vibrational band (**Figure 10*b***) that can be used for specific imaging with CARS. **Figure 10*c*** shows the distribution of a 10% retinol solution applied to mouse ear skin. The drug is seen to localize in the intercellular space between the corneocytes of the stratum corneum, which is a pathway for entry into the dermis (64).

As demonstrated by the brightness of the adipocytes in CARS images (**Figure 9**), adipose tissue yields strong CARS signal. White adipose tissue of a mouse omentum majus, for example, generates intense CARS signals from the large (>50 μm) adipocytes (**Figure 11*a***).

CARS microscopy has also been used to visualize the microstructure of excised mouse lungs (**Figure 11*b***). Lung tissue is primarily composed of small air sacs called alveoli that are coated with a lipid-rich surfactant. CARS images of lung tissue, tuned into the symmetric $CH_2$ stretching vibration, show these alveoli along with numerous

${journal.abbrev} 2008.1:883-909. Downloaded from arjournals.annualreviews.org
by HARVARD UNIVERSITY on 10/14/08. For personal use only.

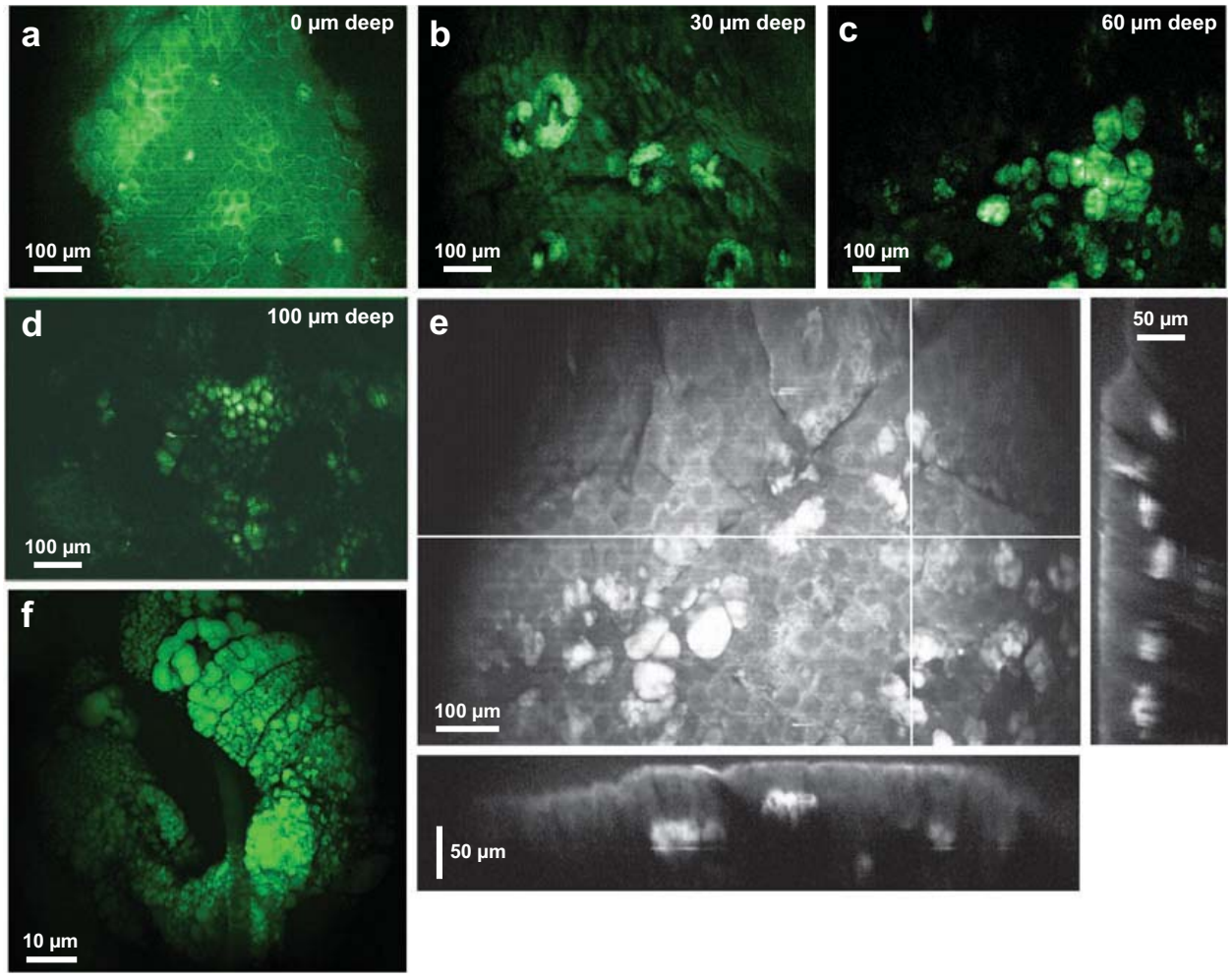


**Figure 9**

Coherent anti-Stokes Raman scattering images of mouse skin at the lipid band (2845 $cm^{-1}$) in vivo. (*a*) The surface of hairless mouse skin imaged at the lipid band. The outlines of the corneocytes are clearly visible due to the lipid-rich intracellular "mortar" of the stratum corneum. (*b*) Sebaceous glands imaged at ~30 μm deep. (*c*) Adipocytes at approximately ~60 μm deep, in the dermis. (*d*) Subcutaneous fat composed of many small adipocytes, nearly 100 μm deep. (*e*) Two-dimensional projection of 60 images from a depth stack taken every 2 μm. *YZ* and *XZ* cross sections (*right* and *bottom* panels, respectively) were constructed from the depth stack along the white lines. The cross sections are presented in inverse contrast to show better detail. (*f*) Three-dimensional rendering of a mouse sebaceous gland. The crescent-shaped sebaceous gland surrounding a hair shaft is composed of multiple cells, each filled with numerous micrometer-sized $CH_2$-rich sebum granules.

lipid-rich cells, most likely surfactant cells (type II pneumoctyes), Clara cells, and macrophages (66, 67).

Tissues of the kidney give excellent contrast when imaged with CARS microscopy. Adipose tissue, visualized on the surface of the kidney, stands out prominently in CARS images taken at the lipid band (**Figure 11*c***). Beneath the kidney surface, at depths of approximately 40 μm, proximal and distal renal tubules are clearly visible

${journal.abbrev} 2008.1:883-909. Downloaded from arjournals.annualreviews.org
by HARVARD UNIVERSITY on 10/14/08. For personal use only.

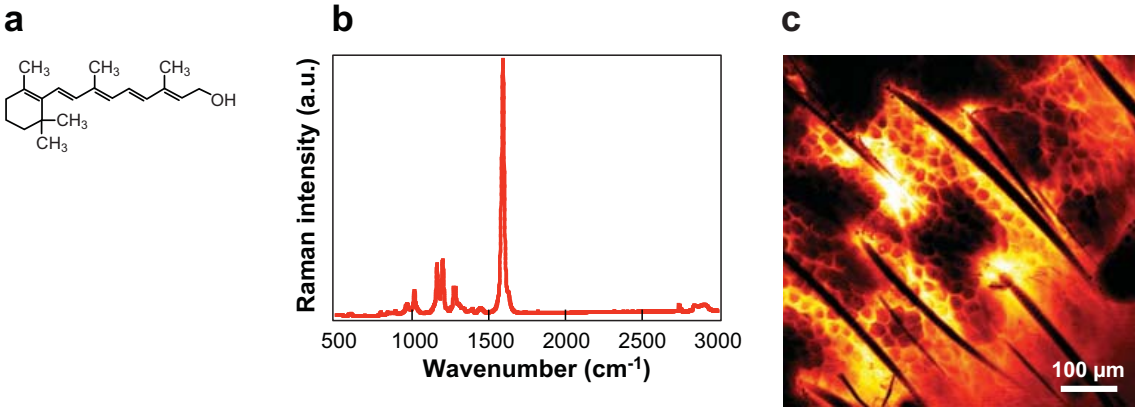


**Figure 10**

(*a*) Structure of retinol. (*b*) Raman spectrum of retinol, showing the strong characteristic peak at 1594 $cm^{-1}$ arising from the conjugated polyene structure. (*c*) 620 μm × 620 μm image of mouse ear skin treated with a 10% retinol in myritol 318 solution. Myritol 318 is a compound typically found in skin creams (65).

(**Figure 11*d***). Close examination of the tubule walls shows the many rounded nuclei of the tubules' epithelial cells, which appear dark due to their low lipid content.

The retina is composed of multiple layers of lipid-rich neurons, each with a different function and microscopic structure that can be readily identified using CARS microscopy (**Figure 11*e***). The photoreceptor, inner and outer nuclear, and inner and outer plexiform layers are easily seen in cross-sectional images. En face CARS depth stacks (**Supplemental Movie 1**; follow the **Supplemental Material link** from the Annual Reviews home page at **http://www.annualreviews.org**) allow full three-dimensional reconstruction of retinal tissue, in which it is possible to visualize the nerve fiber layer and ganglion cells. Capillaries crossing the retina surface, many containing red blood cells, are easily seen with lipid contrast (**Figure 11*f***).

Numerous CARS microscopy studies have focused on nerve bundle structure and function. For example, excised spinal cords have been visualized using the $CH_2$ stretching vibration (68), and the sciatic nerve of living mice has been imaged using minimal surgical techniques (69). Recent studies have even used CARS contrast to study the breakdown of nerve structures in demyelination disorders (70).

A new and exciting biomedical application of CARS microscopy is the imaging of brain tissue (20). Brain tissue is lipid dense as it is composed of billions of neurons and support cells. Using $CH_2$ stretching contrast, CARS microscopy has been used to visualize a number of brain structures. A coronal section of mouse brain, taken 2.8 mm from the bregma, shows a number of brain structures when imaged with CARS microscopy. In order to maintain cellular resolution and image the full organ, the brain mosaics shown were built from individual 700 μm × 700 μm CARS images (**Figure 12*a***). White matter tracts, such as the association fiber bundle in the centrum semiovale, the corpus callosum, and corticospinal tracts, are rich in myelin and give rise to intense lipid band CARS signals. The white matter regions in the diencephalon

${journal.abbrev} 2008.1:883-909. Downloaded from arjournals.annualreviews.org
by HARVARD UNIVERSITY on 10/14/08. For personal use only.

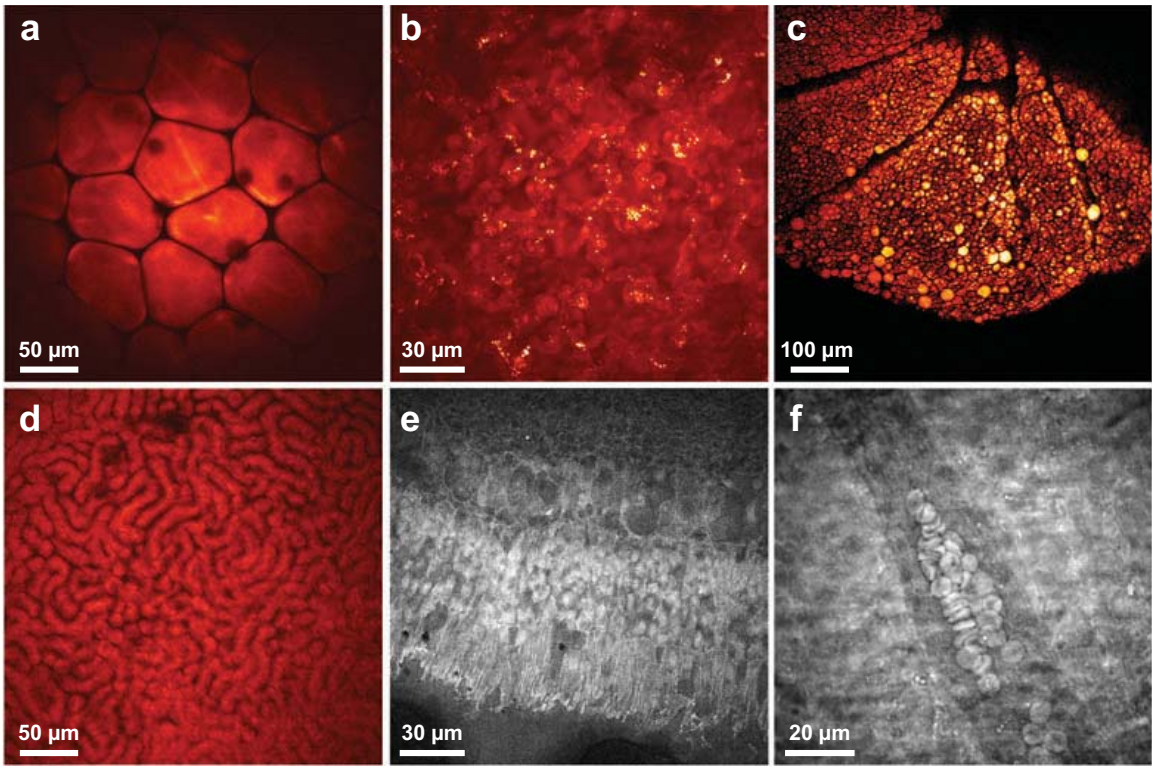


**Figure 11**

Coherent anti-Stokes Raman scattering (CARS) imaging of various tissues ex vivo with $CH_2$ contrast. (*a*) Epi-CARS image of white adipose tissue of mouse omentum majus. These large adipose cells are packed with fatty acids and give rise to strong CARS signals. (*b*) Epi-CARS microscopy of mouse lung tissue, showing the individual alveoli. CARS signals are thought to arise from the lipid-rich surfactant cells, Clara cells, and macrophages. (*c*) Epi-CARS image of the surface of the adipocyte-covered mouse kidney. (*d*) Epi-CARS image of mouse kidney taken at a depth of 40 μm reveals many renal tubules. (*e*) Forward-propagating CARS image of a fixed bovine retina in cross section. The first several layers of the retina can be identified. (*f*) En face epi-CARS image of a fixed human retina taken at the retinal surface. A capillary just above the nerve fiber layer contains numerous erythrocytes.

and deep brain nuclei can also be identified by their CARS signal strength. In order to compare the contrast from lipid band CARS imaging to the gold standard in biological imaging, hematoxylin and eosin (H&E) histological preparations were carried out on CARS-visualized brain samples. **Figure 12*b*** shows a 700 μm × 700 μm image of the corpus callosum and surrounding structures, which are compared with the corresponding H&E-stained section (**Figure 12*c***), demonstrating the gray-white matter contrast and revealing the microstructural anatomical information available from CARS microscopy.

This study also demonstrated the ability of CARS to distinguish healthy and diseased brain tissue (20). A large astrocytoma is readily seen in a lipid band CARS image due to the lipid-poor nature of the tumor (**Figure 12*d***). Close examination of the tumor margins (**Figure 12*e***) reveals the highly invasive nature of the astrocytoma as it infiltrates the surrounding healthy white matter. Such studies open

**H&E:** hematoxylin and eosin

${journal.abbrev} 2008.1:883-909. Downloaded from arjournals.annualreviews.org
by HARVARD UNIVERSITY on 10/14/08. For personal use only.

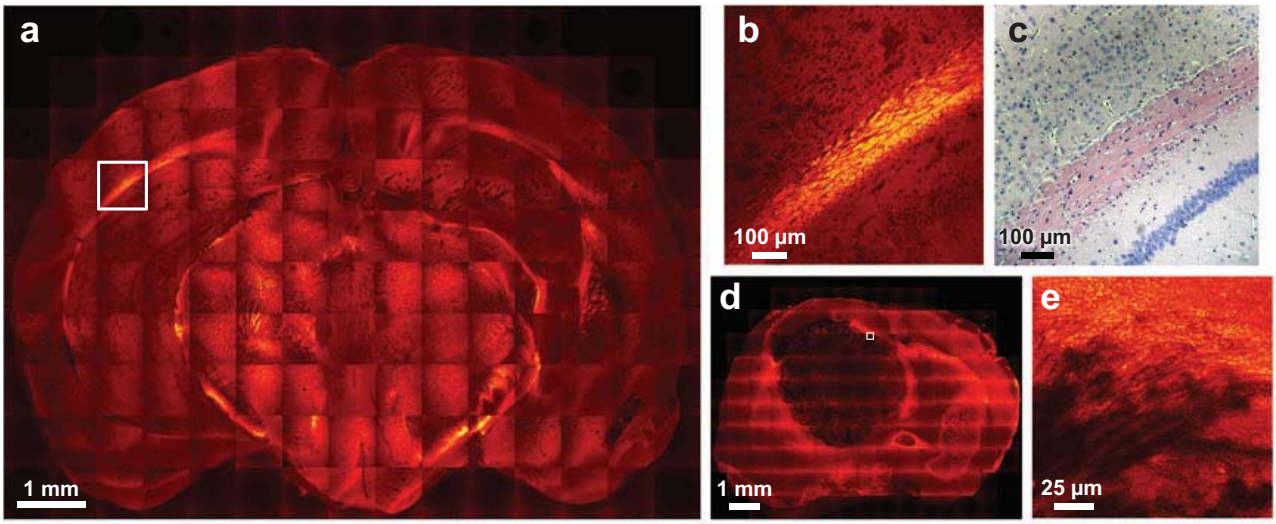


**Figure 12**

Epi-CARS microscopy applied to brain tissue imaging. (*a*) Mosaic image of a mouse brain coronal section taken at the lipid band showing numerous brain structures. (*b*) A single zoomed-in image corresponding to the white box in panel *a*. (*c*) Hematoxylin and eosin (H&E) image of the same region of the same mouse brain. The structures visible in both images, from upper left to bottom right, are the cortex, corpus callosum, oriens layer, and pyramidal layer. The corpus callosum, a myelinated brain structure, gives rise to a strong CARS signal. (*d*) A mosaic CARS image of astrocytoma in a mouse sacrificed four weeks after inoculation with tumor cells. (*e*) A zoomed-in image corresponding to the white box in panel *d* shows tumor infiltration at the margin.

the door to a number of potential clinical applications, wherein CARS microscopy could one day replace traditional histopathology in brain imaging. In particular, a CARS microendoscope (71) offers the ability to probe deep into brain tissue for diagnostic imaging and could reduce the need for brain tissue resectioning in the future.

## 6. THE FUTURE OF COHERENT ANTI-STOKES RAMAN SCATTERING MICROSCOPY

Advances over the past several years have made CARS microscopy a state-of-the-art technique. Its ability to perform label-free chemical imaging is beginning to make contributions to biology and medicine. Current FM-CARS systems are capable of probing several important metabolites. CARS microscopy, specifically the FM-CARS technique, also has the potential to play a large role in drug research as it enables the study of drug localization and uptake at the subcellular level.

Another important application of CARS will be in cancer diagnostics. Tumors often show distinct chemical and morphological differences from their host tissue (72, 73). CARS microscopy is capable of providing chemically specific information along with tissue morphology to identify and study cancerous lesions. CARS can also be combined with other intrinsic imaging techniques such as multiphoton fluorescence

microscopy (74), second harmonic generation microscopy (75), and third harmonic generation microscopy (76) to provide a multimodal platform for tissue diagnostics.

CARS endoscopy will also be used as an in situ surgical probe for tumor margins. A CARS microendoscope, as part of a fiber probe or needle biopsy, could provide a means of sampling a surgical region prior to resection. Such an approach might be applied to the diagnosis of breast tumors, which are characterized by changes in lipid content and morphology (77). The sensitivity of CARS to lipids could also be used to detect and analyze atherosclerotic plaques in situ (78).

In 1999, the use of CARS microscopy to study living systems was just beginning. There has been a vision to move CARS imaging from the laser lab into the hospital, where it could provide direct benefits to patients. At this point, CARS microscopy is well on its way to reaching that goal. Given the creativity and innovation of the ever-growing community of CARS enthusiasts, CARS microscopy will become a valuable tool for biomedicine for many years to come.

${journal.abbrev} 2008.1:883-909. Downloaded from arjournals.annualreviews.org
by HARVARD UNIVERSITY on 10/14/08. For personal use only.

## SUMMARY POINTS

1. CARS microscopy provides chemically selective information by tuning into characteristic vibrational resonances in samples without the use of labels or the complication of photobleaching.
2. The stimulated coherent excitation of many vibrational oscillators gives rise to a much stronger signal than that of conventional Raman microscopy, allowing for real-time imaging of living cells or organisms at tolerable laser powers.
3. The CARS signal is only generated at the focal spot, allowing 3D sectioning of thick tissues.
4. Epi-directed CARS signal is generated via three different mechanisms: incomplete destructive interference by objects smaller than the wavelength of light, discontinuity of the third-order nonlinear susceptibility $\chi^{(3)}$ at the interface of two media, and backscattering of initially forward-propagating photons in turbid specimens.
5. The optimum light source for CARS imaging is a picosecond pulsed laser that operates in the NIR range, preferably above 800 nm to avoid multiphoton damage of specimens and to allow for deep penetration in thick samples.
6. The sensitivity of CARS microscopy has been improved by frequency modulation CARS detection.
7. Isotope substitution by deuterium offers a well-isolated CD stretching frequency for mapping the distribution of metabolites or drugs.
8. As a medical imaging technique, CARS is capable of whole-organ imaging at subcellular resolutions in real time.

${journal.abbrev} 2008.1:883-909. Downloaded from arjournals.annualreviews.org
by HARVARD UNIVERSITY on 10/14/08. For personal use only.

### FUTURE ISSUES

1. What is the ultimate sensitivity of CARS detection?
2. Can fiber delivery and fiber-based laser sources reduce the cost and complexity of CARS microscopy systems?
3. Can the penetration depth of CARS microscopy be extended through adaptive optics?
4. Is it possible to apply the capabilities of CARS to intraoperative endoscopy?

## DISCLOSURE STATEMENT

Patents and patent applications held by X.S.X. have been licensed to multiple microscope manufacturers.

## ACKNOWLEDGMENTS

We would like to extend a special thanks to our collaborators who have made much of this work possible. Prof. Charles Lin and his colleagues Prof. Daniel Côté and Dr. Mehron Pouris'haag at Massachusetts General Hospital were instrumental in developing video-rate CARS microscopy for skin imaging. Dr. Robert Farris of the National Institutes of Health Eye Institute provided retina samples. Dr. Geoffrey Young, Prof. Stephen Wong, Dr. Xiaoyin Xu, and Dr. Santosh Kesari of Harvard Medical School were collaborators in the brain imaging work. Prof. Zemin Yao at the University of Ottawa was our key collaborator in the lipid metabolism study. We worked closely with Prof. John Pezaski's group at the National Research Council in Ottawa on the hepatitis C projects. Dr. Yiwei Jia of Olympus was of critical assistance in building our first beam-scanning CARS microscope, and has been a very helpful colleague. Dr. Christa Ackermann of Pfizer has worked closely with us on the development of the next-generation FM-CARS system with funding from the Pfizer corporation. Dr. Shuliang Zhang of Unilever has collaborated on several imaging projects with funding from the Unilever Corporation.

We must also acknowledge many Xie group members, past and present, whose hard work and dedication made the many advances presented here possible: Prof. Andreas Zumbush, Dr. Gary Holtom, Dr. Andreas Volkmer, Dr. Lewis Book, Prof. Ji-Xin Cheng, Prof. Eric O. Potma, Prof. François Légaré, Prof. Feruz Ganikhanov, Dr. Silvia Carrasco, Dr. Xiaolin Nan, Dr. Wei Yuan Yang, Brian G. Saar, and Christian Freudiger. Funding for the development of CARS microscopy has come from the National Institutes of Health (R01 GM62536–02), the National Science Foundation (DBI-0649892, DBI-0138028) and a National Institutes of Health Director's Pioneer Award awarded to X.S.X. C.L.E. wishes to acknowledge the National Science Foundation for a Graduate Research Fellowship.

## LITERATURE CITED

1. Zipfel WR, Williams RM, Christie R, Nikitin AY, Hyman BT, Webb WW. 2003. Live tissue intrinsic emission microscopy using multiphoton-excited native

${journal.abbrev} 2008.1:883-909. Downloaded from arjournals.annualreviews.org
by HARVARD UNIVERSITY on 10/14/08. For personal use only.

fluorescence and second harmonic generation. *Proc. Natl. Acad. Sci.* 100:7075–80

2. Miller L, Smith G, Carr G. 2003. Synchrotron-based biological microspectroscopy: from the mid-infrared through the far-infrared regimes. *J. Biol. Phys.* 29:219–30
3. Berger A, Itzkan I, Feld M. 1997. Feasibility of measuring blood glucose concentration by near-infrared Raman spectroscopy. *Spectrochim. Acta A Mol. Biomol. Spectrosc.* 53:287–92
4. Huang Z, McWilliams A, Lui H, McLean DI, Lam S, Zeng H. 2003. Near-infrared Raman spectroscopy for optical diagnosis of lung cancer. *Int. J. Cancer* 107:1047–52
5. Nijssen A, Bakker Schut TC, Heule F, Caspers PJ, Hayes DP, et al. 2002. Discriminating basal cell carcinoma from its surrounding tissue by Raman spectroscopy. *J. Invest. Dermatol.* 119:64–69
6. Cao Y, Jin R, Mirkin C. 2002. Nanoparticles with Raman spectroscopic fingerprints for DNA and RNA detection. *Science* 297:1536–40
7. Shim MG, Song LMWK, Marcon NE, Wilson BC. 2000. In vivo near-infrared Raman spectroscopy: demonstration of feasibility during clinical gastrointestinal endoscopy. *Photochemistry Photobiol.* 72:146–50
8. van Manen HJ, Kraan YM, Roos D, Otto C. 2005. Single-cell Raman and fluorescence microscopy reveal the association of lipid bodies with phagosomes in leukocytes. *Proc. Natl. Acad. Sci.* 102:10159–64
9. Maker PD, Terhune RW. 1965. Study of optical effects due to an induced polarization third order in the electric field strength. *Phys. Rev.* 137:A801–18
10. Begley RF, Harvey AB, Byer RL. 1974. Coherent anti-Stokes Raman scattering. *Appl. Phys. Lett.* 25:387–90
11. Duncan MD, Reintjes J, Manuccia TJ. 1982. Scanning coherent anti-Stokes Raman microscope. *Opt. Lett.* 7:350–52
12. Zumbusch A, Holtom GR, Xie XS. 1999. Three-dimensional vibrational imaging by coherent anti-Stokes Raman scattering. *Phys. Rev. Lett.* 82:4142–45
13. Cheng JX, Jia YK, Zheng G, Xie XS. 2002. Laser-scanning coherent anti-Stokes Raman scattering microscopy and applications to cell biology. *Biophys. J.* 83:502–9
14. Dufresne ER, Corwin EI, Greenblatt NS, Ashmore J, Wang DY, et al. 2003. Flow and fracture in drying nanoparticle suspensions. *Phys. Rev. Lett.* 91:224501
15. Nan X, Yang WY, Xie XS. 2004. CARS microscopy: lights up lipids in living cells. *Biophotonics Int.* 11:44
16. Nan X, Potma EO, Xie XS. 2006. Nonperturbative chemical imaging of organelle transport in living cells with coherent anti-Stokes Raman scattering microscopy. *Biophys. J.* 91:728–35
17. Potma EO, Xie XS. 2003. Detection of single lipid bilayers in coherent anti-Stokes Raman scattering (CARS) microscopy. *J. Raman Spectrosc.* 34:642–50
18. Potma EO, Xie XS. 2005. Direct visualization of lipid phase segregation in single lipid bilayers with coherent anti-Stokes Raman scattering microscopy. *Chem. Phys. Chem.* 6:77–79

${journal.abbrev} 2008.1:883-909. Downloaded from arjournals.annualreviews.org
by HARVARD UNIVERSITY on 10/14/08. For personal use only.

19. Evans CL, Potma EO, Puoris'haag M, Cote D, Lin CP, Xie XS. 2005. Chemical imaging of tissue in vivo with video-rate coherent anti-Stokes Raman scattering microscopy. *Proc. Natl. Acad. Sci. USA* 102:16807–12
20. Evans CL, Xu X, Kesari S, Xie XS, Wong STC, Young GS. 2007. Chemically-selective imaging of brain structures with CARS microscopy. *Opt. Expr.* 15:12076–87
21. Evans CL, Potma EO, Xie XS. 2004. Coherent anti-Stokes Raman scattering spectral interferometry: determination of the real and imaginary components of nonlinear susceptibility $\chi^{(3)}$ for vibrational microscopy. *Opt. Lett.* 29:2923–25
22. Potma EO, Evans CL, Xie XS. 2006. Heterodyne coherent anti-Stokes Raman scattering (CARS) imaging. *Opt. Lett.* 31:241–43
23. Ganikhanov F, Evans CL, Saar BG, Xie XS. 2006. High sensitivity vibrational imaging with frequency modulation coherent anti-Stokes Raman scattering (FM-CARS) microscopy. *Opt. Lett.* 31:1872–74
24. Hellwarth RW. 1977. Third-order optical susceptibilities of liquids and solids. *Prog. Quantum Electron.* 5:1–68
25. Maeda S, Kamisuki T, Adachi Y. 1988. Condensed phase CARS. In *Advances in Non-Linear Spectroscopy*, ed. RJH Clark, RE Hester, pp. 253–97. New York: Wiley
26. Lin-Vien D, Colthup NB, Fateley WG, Grasselli JG. 1991. *The Handbook of Infrared and Raman Characteristic Frequencies of Organic Molecules*. San Diego: Academic
27. Wurpel GWH, Schins JW, Müller M. 2002. Chemical specificity in 3D imaging with multiplex CARS microscopy. *Opt. Lett.* 27:1093–95
28. Cheng JX, Volkmer A, Book LD, Xie XS. 2002. Multiplex coherent anti-Stokes Raman scattering microspectroscopy and study of lipid vesicles. *J. Phys. Chem. B.* 106:8493–98
29. Kee TW, Cicerone MT. 2004. Simple approach to one-laser, broadband coherent anti-Stokes Raman scattering microscopy. *Opt. Lett.* 29:2701–3
30. Lim SH, Caster AG, Leone SR. 2005. Single-pulse phase-control interferometric coherent anti-Stokes Raman scattering spectroscopy. *Phys. Rev. A* 72:41803
31. Vartiainen EM, Rinia HA, Müller M, Bonn M. 2006. Direct extraction of Raman line-shapes from congested CARS spectra. *Opt. Expr.* 14:3622–30
32. Oron D, Dudovich N, Silberberg Y. 2003. Femtosecond phase-and-polarization control for background-free coherent anti-Stokes Raman spectroscopy. *Phys. Rev. Lett.* 90:213902
33. Frumker E, Oron D, Mandelik D, Silberberg Y. 2004. Femtosecond pulse-shape modulation at kilohertz rates. *Opt. Lett.* 29:890–92
34. Frumker E, Tal E, Silberberg Y, Majer D. 2005. Femtosecond pulse-shape modulation at nanosecond rates. *Opt. Lett.* 30:2796–98
35. Cheng JX, Volkmer A, Xie XS. 2002. Theoretical and experimental characterization of coherent anti-Stokes Raman scattering microscopy. *J. Opt. Soc. Am. B* 19:1363–75
36. Boyd RW. 2003. *Nonlinear Optics*. London: Academic
37. Potma EO, Boeij WPD, Wiersma DA. 2000. Nonlinear coherent four-wave mixing in optical microscopy. *J. Opt. Soc. Am. B* 17:1678–84

${journal.abbrev} 2008.1:883-909. Downloaded from arjournals.annualreviews.org
by HARVARD UNIVERSITY on 10/14/08. For personal use only.

38. Cheng J, Volkmer A, Book LD, Xie XS. 2001. An epi-detected coherent anti-Stokes Raman scattering (E-CARS) microscope with high spectral resolution and high sensitivity. *J. Phys. Chem. B* 105:1277–80
39. Fu Y, Wang H, Shi R, Cheng JX. 2006. Characterization of photodamage in coherent anti-Stokes Raman scattering microscopy. *Opt. Expr.* 14:3942–51
40. Beaurepaire E, Oheim M, Mertz J. 2001. Ultra-deep two-photon fluorescence excitation in turbid media. *Opt. Commun.* 188:25–29
41. Ganikhanov F, Carrasco S, Xie XS, Katz M, Seitz W, Kopf D. 2006. Broadly tunable dual-wavelength light source for coherent anti-Stokes Raman scattering microscopy. *Opt. Lett.* 31:1292–94
42. Potma EO, Jones DJ, Cheng JX, Xie XS, Ye J. 2002. High-sensitivity coherent anti-Stokes Raman microscopy with two tightly synchronized picosecond lasers. *Opt. Lett.* 27:1168–70
43. Jones DJ, Potma EO, Cheng JX, Burfeindt B, Pang Y, et al. 2002. Synchronization of two passively mode-locked, ps lasers within 20 fs for coherent anti-Stokes Raman scattering microscopy. *Rev. Sci. Instrum.* 73:2843–48
44. Cheng JX, Book LD, Xie XS. 2001. Polarization coherent anti-Stokes Raman scattering microscopy. *Opt. Lett.* 26:1341–43
45. Volkmer A, Cheng J, Xie XS. 2001. Vibrational imaging with high sensitivity via epi-detected coherent anti-Stokes Raman scattering microscopy. *Phys. Rev. Lett.* 87:23901
46. Volkmer A, Book LD, Xie XS. 2002. Time-resolved coherent anti-Stokes Raman scattering microscopy: imaging based on Raman free induction decay. *Appl. Phys. Lett.* 80:1505–7
47. Andresen ER, Keiding SR, Potma EO. 2006. Picosecond anti-Stokes generation in a photonic-crystal fiber for interferometric CARS microscopy. *Opt. Expr.* 14:7246–51
48. Potma EO, Xie XS. 2003. Detection of single lipid bilayers with coherent anti-Stokes Raman scattering (CARS) microscopy. *J. Raman Spectrosc.* 34:642–50
49. Wurpel GWH, Rinia HA, Muller M. 2005. Imaging orientational order and lipid density in multilamellar vesicles with multiplex CARS microscopy. *J. Microsc.* 218:37–45
50. Wurpel GWH, Schins JM, Müller M. 2004. Direct measurement of chain order in single phospholipid mono- and bilayers with multiplex CARS. *J. Phys. Chem. B* 108:3400–3
51. Potma EO, Xie XS, Muntean L, Preusser J, Jones D, et al. 2004. Chemical imaging of photoresists with coherent anti-Stokes Raman scattering (CARS) microscopy. *J. Phys. Chem. B* 108:1296–1301
52. Dufresne ER, Corwin EI, Greenblatt NA, Ashmore J, Wang DY, et al. 2003. Flow and fracture in drying nanoparticle suspensions. *Phys. Rev. Lett.* 91:224501
53. Saar BG, Park H-S, Xie XS, Lavrentovich OD. 2007. Three-dimensional imaging of chemical bond orientation in liquid crystals by coherent anti-Stokes Raman scattering microscopy. *Opt. Expr.* 15(21):13585–96
54. Schliwa M, Woehlke G. 2001. Molecular motors: switching on kinesin. *Nature* 411:424–25

${journal.abbrev} 2008.1:883-909. Downloaded from arjournals.annualreviews.org
by HARVARD UNIVERSITY on 10/14/08. For personal use only.

55. Vale RD. 2003. The molecular motor toolbox for intracellular transport. *Cell* 112:467–80
56. Murphy DJ. 2001. The biogenesis and functions of lipid bodies in animals, plants and microorganisms. *Prog. Lipid Res.* 40:325–438
57. Liu P, Ying Y, Zhao Y, Mundy DI, Zhu M, Anderson RGW. 2004. Chinese hamster ovary K2 cell lipid droplets appear to be metabolic organelles involved in membrane traffic. *J. Biol. Chem.* 279:3787–92
58. Fujimoto Y, Itabe H, Sakai J, Makita M, Noda J, et al. 2004. Identification of major proteins in the lipid droplet–enriched fraction isolated from the human hepatocyte cell line HuH7. *Biochim. Biophys. Acta Mol. Cell Res.* 1644:47–59
59. Fukumoto S, Fujimoto T. 2002. Deformation of lipid droplets in fixed samples. *Histochem. Cell Biol.* 118:423–28
60. Rakic B, Sagan SM, Noestheden M, Belanger S, Nan X, et al. 2006. Peroxisome proliferator–activated receptor $\alpha$ antagonism inhibits hepatitis C virus replication. *Chem. Biol.* 13:23–30
61. Nan X, Tonary AM, Stolow A, Xie XS, Pezacki JP. 2006. Intracellular imaging of HCV RNA and cellular lipids by using simultaneous two-photon fluorescence and coherent anti-Stokes Raman scattering microscopies. *ChemBioChem* 7:1895–97
62. Hellerer T, Axang C, Brackmann C, Hillertz P, Pilon M, Enejder A. 2007. Monitoring of lipid storage in *Caenorhabditis elegans* using coherent anti-Stokes Raman scattering (CARS) microscopy. *Proc. Natl. Acad. Sci.* 104:14658–63
63. Xie XS, Yu J, Yang WY. 2006. Living cells as test tubes. *Science* 312:228–30
64. Pudney PDA, Melot M, Caspers PJ, Van Der Pol A, Puppels GJ. 2007. An in vivo confocal Raman study of the delivery of trans-retinol to the skin. *Appl. Spectrosc.* 61:804–11
65. Barry BW. 1991. Lipid-protein-partitioning theory of skin penetration enhancement. *J. Control. Release* 15:237–48
66. Young B, Heath JW. 2000. *Wheater's Functional Histology: A Text and Colour Atlas.* London: Churchill Livingstone
67. Heinrich C, Bernet S, Ritsch-Marte M. 2007. Wide-field coherent anti-Stokes Raman scattering microscopy with non-phase-matching illumination. *Opt. Lett.* 32:3468–69
68. Wang H, Fu Y, Zickmund P, Shi R, Cheng JX. 2005. Coherent anti-Stokes Raman scattering imaging of axonal myelin in live spinal tissues. *Biophys. J.* 89:581–91
69. Huff TB, Cheng JX. 2007. In vivo coherent anti-Stokes Raman scattering imaging of sciatic nerve tissue. *J. Microsc.* 225:175–82
70. Fu Y, Wang H, Huff TB, Shi R, Cheng JX. 2007. Coherent anti-Stokes Raman scattering imaging of myelin degradation reveals a calcium-dependent pathway in lyso-PtdCho-induced demyelination. *J. Neurosci. Res.* 85:2870–81
71. Légaré F, Evans CL, Ganikhanov F, Xie XS. 2006. Towards CARS endoscopy. *Opt. Expr.* 14:4427–32
72. Haka AS, Shafer-Peltier KE, Fitzmaurice M, Crowe J, Dasari RR, Feld MS. 2005. Diagnosing breast cancer by using Raman spectroscopy. *Proc. Natl. Acad. Sci.* 102:12371–76

73. Gniadecka M, Philipsen PA, Sigurdsson S, Wessel S, Nielsen OF, et al. 2004. Melanoma diagnosis by Raman spectroscopy and neural networks: structure alterations in proteins and lipids in intact cancer tissue. *J. Invest. Dermatol.* 122: 443–49
74. Zipfel WR, Williams RM, Webb WW. 2003. Nonlinear magic: multiphoton microscopy in the biosciences. *Nat. Biotechnol.* 21:1369–77
75. Campagnola PJ, Millard AC, Terasaki M, Hoppe PE, Malone CJ, Mohler WA. 2002. Three-dimensional high-resolution second-harmonic generation imaging of endogenous structural proteins in biological tissues. *Biophys. J.* 81:493–508
76. Squier JA, Muller M, Brakenhoff GJ, Wilson KR. 1998. Third harmonic generation microscopy. *Opt. Expr.* 3:315–24
77. Shafer-Peltier KE, Haka AS, Fitzmaurice M, Crowe J, Myles J, et al. 2002. Raman microspectroscopic model of human breast tissue: implications for breast cancer diagnosis in vivo. *J. Raman Spectrosc.* 33:552–63
78. Le TT, Langohr IM, Locker MJ, Sturek M, Cheng JX. 2007. Label-free molecular imaging of atherosclerotic lesions using multimodal nonlinear optical microscopy. *J. Biomed. Opt.* 12:054007
79. Thomas GJ Jr. 1999. Raman spectroscopy of protein and nucleic acid assemblies. *Ann. Rev. Biophys. Biomol. Struct.* 28:1–27

${journal.abbrev} 2008.1:883-909. Downloaded from arjournals.annualreviews.org
by HARVARD UNIVERSITY on 10/14/08. For personal use only.

Annual Review of Analytical Chemistry

Volume 1, 2008

# Contents





${journal.abbrev} 2008.1:883-909. Downloaded from arjournals.annualreviews.org
by HARVARD UNIVERSITY on 10/14/08. For personal use only.

${journal.abbrev} 2008.1:883-909. Downloaded from arjournals.annualreviews.org
by HARVARD UNIVERSITY on 10/14/08. For personal use only.

${journal.abbrev} 2008.1:883-909. Downloaded from arjournals.annualreviews.org
by HARVARD UNIVERSITY on 10/14/08. For personal use only.